

Nonlinear effects for island coarsening and stabilization during strained film heteroepitaxy

Champika G. Gamage and Zhi-Feng Huang

Department of Physics and Astronomy, Wayne State University, Detroit, Michigan 48201, USA

(Dated: October 18, 2018)

Nonlinear evolution of three-dimensional strained islands or quantum dots in heteroepitaxial thin films is studied via a continuum elasticity model and the development of a nonlinear dynamic equation governing the film morphological profile. All three regimes of island array evolution are identified and examined, including a film instability regime at early stage, a nonlinear coarsening regime at intermediate times, and the crossover to a saturated asymptotic state, with detailed behavior depending on film-substrate misfit strains but not qualitatively on finite system sizes. The phenomenon of island stabilization and saturation, which corresponds to the formation of steady but non-ordered arrays of strained quantum dots, occurs at later time for smaller misfit strain. It is found to be controlled by the strength of film-substrate wetting interaction which would constrain the valley-to-peak mass transport and hence the growth of island height, and also determined by the effect of elastic interaction between surface islands and the high-order strain energy of individual islands at late evolution stage. The results are compared to previous experimental and theoretical studies on quantum dots coarsening and saturation.

PACS numbers: 81.15.Aa, 68.55.-a, 68.65.Hb

I. INTRODUCTION

The formation of surface nanostructures such as islands or quantum dots during heteroepitaxy of strained films has attracted continuing great interest, due to its importance in both fundamental understanding of material growth and its wide range of applications particularly for optoelectronic nano devices¹⁻³. One of the underlying mechanisms of island formation has been attributed to the occurrence of morphological instability of the strained film (i.e., the Asaro-Tiller-Grinfeld instability⁴), for which the competition between the stabilization effect of film surface energy and the destabilization effect of system elastic energy due to film-substrate misfit strain plays a key role. This involves the procedure of stress release in the film via surface mass transport driven by local energy gradient and consequently the formation of coherent nonplanar surface structures like nanoscale islands^{5,6}. Compared to other formation mechanisms such as thermally activated nucleation, a main feature here is the continuous, nucleationless nature of the film instability and the subsequent island growth that starts from rough surface⁷⁻⁹. It results in more regular and correlated arrays of self assembled quantum dots that are appealing for a variety of applications.

The onset of this type of quantum dots or strained islands formation has been well understood, as studied via detailed instability analysis for both single-component^{5,6} and alloy strained films¹⁰⁻¹³ as well as multilayers/superlattices^{14,15}. Such film instability, showing as surface ripples and cell-like undulations which are the precursor of coherent island formation, has been observed in experiments of semiconductor heteroepitaxial films such as SiGe^{7,8}. On the other hand, the subsequent nonlinear evolution of these strained dots that are well beyond the initial linear stability stage, is more complicated and much less understood. A typical phenomenon is the coarsening of quantum dot islands, showing as the increase of average island size during film evolution and the shrinking of small dots. Such scenario has been observed in experiments of Ge/Si(001)¹⁶⁻¹⁹, SiGe/Si(001)²⁰, and InAs/GaAs(001)²¹, although with different mechanisms and behavior of coarsening reported. For the example of Ge-Si systems that have been extensively studied, nonlinear island coarsening rate that deviates from classical results of Ostwald ripening has been found; however, it was associated with different mechanisms of island morphology evolution in different experiments, such as the effect of island shape transition accompanying the coarsening process¹⁶⁻¹⁸ or a contrasting kinetic picture that incorporates elastic interactions but not island shape transition²⁰. Also, the slowing¹⁶ or suppression¹⁹ of coarsening process at late stage and the resulting saturated, stabilized quantum dot arrays^{17,19,22} have been observed in some experiments, but not others²⁰.

The corresponding theoretical/computational study on nonlinear island evolution is also far from conclusive. Most efforts are based on continuum approaches including continuum elasticity theory²³⁻³⁵ and phase field methods^{37,38}, in addition to other modeling techniques that incorporate crystalline details, such as kinetic Monte Carlo method with elastic interaction³⁹⁻⁴¹ and the recently developed phase-field-crystal (PFC) model and the associated amplitude equation formalism⁴²⁻⁴⁵. For continuum elasticity modeling, which is the current main avenue for studying strained island coarsening due to the large length and time scales involved, much recent focus has been put on the derivation and simulation of nonlinear evolution equations through approximating the system elasticity and the dynamics of film morphology via perturbation methods. Two limits of system configuration were addressed in early studies of such

approach, including the limit of perfectly rigid substrate^{24,30} and the case of infinitely thick strained film²⁸. More recently, similar approximation has been applied to heteroepitaxial systems consisting of a strained thin film grown on an elastic substrate as configured in most experiments. The corresponding reduced nonlinear evolution equations have been derived and simulated, based on the long-wave or small-slope approximation of film surface profile^{31,34,35} or the assumption of small surface gradient³³. Some physical mechanisms in thin film growth have also been incorporated, such as the wetting effect between the strained film and the underlying substrate. These approaches are more efficient for large scale simulations, as compared to directly solving the full system elasticity problem and the corresponding full dynamic equation of morphological profile, which instead is of high computational cost and hence usually involves limited system size, island number, and evolution time particularly for three-dimensional (3D) systems.

Despite the success of these theoretical approaches in describing properties of quantum dot formation and film morphology, some behavior of film nonlinear evolution, particularly the process of island coarsening vs. saturation, is still not well understood, with inconsistent results given in different studies^{26,29,32-36}. For the case of film annealing as examined in most simulations, coarsening of strained island arrays has been reproduced, although with different coarsening rate found in different approaches^{29,34,35}. One of the main difference in these work is the result for asymptotic and steady state of the film morphology. Stable arrays of quantum dots that persist after the coarsening stage have been obtained in both studies of the reduced nonlinear evolution equation^{33,36} and the direct solution of the full elasticity problem^{26,32}, consistent with the observation in some Si-Ge experiments^{17,19,22}. However, as in some other experiments²⁰ such scenario of the suppression or cessation of island coarsening was not found in other modeling processes^{29,34}, and recent nonlinear analysis of a system evolution equation suggested that a regular quantum dot array would be unstable as a result of subcritical bifurcation³⁴. Note that in many previous studies the saturation of coarsening islands has been attributed to the effect of surface energy anisotropy^{26,32,36}, although the saturation phenomenon has also been observed in recent simulation without such anisotropy effect³³. These discrepancies in modeling results could probably be related to different types of approximation and various ways of small variable expansion and truncation involved in the approaches, and/or the difficulty in simulating large enough system size and long enough evolution time required for experimental comparison.

In this paper we focus on the nonlinear evolution of strained quantum dot islands grown epitaxially on an elastic substrate, based on a continuum elasticity model and the development of a systematic approach for approximately solving the film-substrate elastic state via a perturbation analysis in Fourier space. Results up to second- and third-order perturbation of surface morphology are presented, and our approach can be readily extended to incorporate higher-order solutions. We can then derive a new nonlinear evolution equation governing the dynamics of strained film morphology, which allows us to systematically examine the detailed behavior of island evolution at large enough spatial and temporal scales. This nonlinear equation, with the incorporation of the wetting effect and also a second-order truncation in the elastic solution, is applied to the study of the coarsening and saturating process in post-deposited, annealing films. Our focus is on systems of small misfit strains, which correspond to large enough length scale of the resulting surface structure as compared to the scale of crystalline lattice. (This is based on recent studies⁴³ showing that continuum approaches, such as the continuum elasticity theory developed here, can well describe the films in weak strain limit, but not for large misfit stress which would lead to qualitatively different behavior of surface islands due to the effects of discrete lattice structure.) The whole series of island evolution can be reproduced in our numerical simulations, including three characteristic regimes: the development of morphological instability and island formation at early times, nonlinear coarsening of islands at intermediate stage, and the slowing of such coarsening process which leads to a saturated state of steady quantum dot arrays. We also investigate the mechanisms underlying the phenomenon of island stabilization and saturation, based on the study of wetting effect on the constraint of surface mass transport between island valleys and peaks, and also on a detailed examination of strain relaxation process via studying the temporal evolution and spatial distribution of elastic energy density at the film surface. We identify a new factor responsible for suppressing the island growth and coarsening, which is attributed to the effect of high-order elastic energy of individual islands and the elastic interaction between them.

II. MODEL

Assume that a strained film of spatially varying height $h(x, y, t)$ is deposited epitaxially on a semi-infinite elastic substrate that occupies the region $z < 0$. The misfit strain in the film with respect to the substrate is given by $\epsilon = (a_f - a_s)/a_s$, where a_f and a_s are the lattice spacings of the film and the substrate respectively. For such coherent, dislocation-free system, the evolution of the film surface morphological profile $h(x, y, t)$ is governed by

$$\frac{\partial h}{\partial t} = \Gamma_h \sqrt{g} \nabla_s^2 \frac{\delta \mathcal{F}}{\delta h} + v, \quad (1)$$

where Γ_h is the kinetic coefficient determined by surface diffusion, ∇_s^2 is the surface Laplacian, v is the deposition rate, and $g = 1 + |\nabla h|^2$. Here the effect of film-substrate interdiffusion is neglected. The total free energy functional \mathcal{F} consists of two parts, including the elastic energy $\mathcal{F}_{el} = \int_{-\infty}^h d^3r \mathcal{E}$ where \mathcal{E} represents the strain energy density, and the surface free energy $\mathcal{F}_s = \int d^2r \gamma_s(h) \sqrt{g}$ where γ_s is the thickness-dependent, isotropic surface tension with the effect of wetting interaction between the film and substrate incorporated. The dynamic equation (1) can then be rewritten as^{6,31,34}

$$\frac{\partial h}{\partial t} = \Gamma_h \sqrt{g} \nabla_s^2 [\gamma \kappa + W(h) + \mathcal{E}^f] + v, \quad (2)$$

where κ is the mean surface curvature, γ is the surface energy density, \mathcal{E}^f gives the film elastic energy density at the surface $z = h$, and the wetting potential W can be approximated via a phenomenological glued-layer wetting model³⁴

$$W(h) = -w \left(\frac{h}{h_{ml}} \right)^{-\alpha_w} e^{-h/h_{ml}}. \quad (3)$$

Here w gives the strength of the film-substrate wetting interaction, h_{ml} is the characteristic wetting-layer thickness that is usually of few monolayers, and the exponent $\alpha_w (> 0)$ gives the singularity of the potential W in the limit of $h \rightarrow 0$ that emulates the persistence of the wetting layer during film evolution³⁴.

The formulation of elasticity for this film-substrate system has been well established⁶. In isotropic, linear elasticity theory (i.e., with harmonic approximation), the elastic energy density is given by $\mathcal{E} = \frac{1}{2} \sigma_{ij} u_{ij}$, where $i, j = x, y, z$, and u_{ij} is the linear elastic strain tensor defined by $u_{ij} = (\partial_j u_i + \partial_i u_j)/2$ (with u_i the displacement field). From Hooke's law for isotropic elastic system, the stress tensor σ_{ij} in the strained film is expressed by

$$\sigma_{ij} = 2\mu \left[\frac{\nu}{1-2\nu} \delta_{ij} u_{kk} + u_{ij} - \frac{1+\nu}{1-2\nu} \epsilon \delta_{ij} \right], \quad (4)$$

where μ is the shear modulus and ν is the Poisson ratio. The stress tensor in the substrate is also given by Eq. (4) with $\epsilon = 0$. Here for simplicity we have assumed equal elastic constants in the film and substrate, which corresponds to the situation in most experimental systems where the difference of elastic constants between film and substrate materials is not significant.

Since the elastic relaxation occurs at a time scale of orders of magnitude faster than that of the atomic diffusion process and the associated system morphological evolution, it is usually assumed that the mechanical equilibrium condition $\partial_j \sigma_{ij} = 0$ is always satisfied in both film and substrate. Using Eq. (4) we can obtain Navier's equations in the whole film-substrate system

$$(1-2\nu) \partial_j^2 u_i + \partial_i \partial_j u_j = 0. \quad (5)$$

The corresponding boundary condition on the top film surface is given by

$$\sigma_{ij}^f n_j = 0 \quad \text{at } z = h(x, y, t), \quad (6)$$

due to the neglecting of external pressure on the free surface, while the boundary conditions at the film-substrate interface is determined by the continuity of stress and displacement fields:

$$\sigma_{ij}^f n_j = \sigma_{ij}^s n_j \quad \text{and} \quad u_i^f = u_i^s \quad \text{at } z = 0. \quad (7)$$

Here n_j is the unit vector normal to the film surface or the film-substrate interface, and the subscripts "f" and "s" refer to the film and substrate phases, respectively. Also, inside the substrate region which is far away from the film we have

$$u_i^s, u_{ij}^s \rightarrow 0 \quad \text{for } z \rightarrow -\infty. \quad (8)$$

III. PERTURBATION ANALYSIS AND NONLINEAR EVOLUTION EQUATION

To solve this elasticity problem, we adopt a perturbation analysis in Fourier space based on the expansion of the small vertical variation of film surface profile. More specifically, given the Fourier transform of the film morphological profile

$$h = \bar{h} + \sum_{\mathbf{q}} \hat{h}(\mathbf{q}, t) e^{i(q_x x + q_y y)}, \quad (9)$$

where $\bar{h} = h_0 + vt$ is the average film thickness at any time t (with h_0 the initial film thickness), the Fourier components of the displacement field $\hat{u}_i(\mathbf{q})$, stress tensor $\hat{\sigma}_{ij}(\mathbf{q})$ ($i, j = x, y, z$), and film elastic energy density $\hat{\mathcal{E}}^f$ are expanded in the order of surface perturbation $\hat{h}(\mathbf{q})$, i.e.,

$$\begin{aligned} u_i &= \bar{u}_i + \sum_{\mathbf{q}} \hat{u}_i(\mathbf{q}) e^{i(q_x x + q_y y)}, & \hat{u}_i &= \hat{u}_i^{(1)} + \hat{u}_i^{(2)} + \hat{u}_i^{(3)} + \dots, \\ \sigma_{ij} &= \bar{\sigma}_{ij} + \sum_{\mathbf{q}} \hat{\sigma}_{ij}(\mathbf{q}) e^{i(q_x x + q_y y)}, & \hat{\sigma}_{ij} &= \hat{\sigma}_{ij}^{(1)} + \hat{\sigma}_{ij}^{(2)} + \hat{\sigma}_{ij}^{(3)} + \dots, \\ \mathcal{E}^f &= \bar{\mathcal{E}}^f + \sum_{\mathbf{q}} \hat{\mathcal{E}}^f(\mathbf{q}) e^{i(q_x x + q_y y)}, & \hat{\mathcal{E}}^f &= \hat{\mathcal{E}}^{(1)f} + \hat{\mathcal{E}}^{(2)f} + \hat{\mathcal{E}}^{(3)f} + \dots. \end{aligned} \quad (10)$$

For the 0th-order base state with planar, uniformly strained film, the elasticity solutions are given by⁶: $\bar{u}_i^f = 0$ ($i = x, y$) and $\bar{u}_z^f = \bar{u}_{zz}^f z$ for the displacement fields, the strain tensor $\bar{u}_{ij}^f = 0$ except for $\bar{u}_{zz}^f = \epsilon(1 + \nu)/(1 - \nu)$, the stress tensor $\bar{\sigma}_{ij}^f = 0$ except for $\bar{\sigma}_{xx}^f = \bar{\sigma}_{yy}^f = -2\mu u_{zz}^0$, and the 0th-order elastic energy density $\bar{\mathcal{E}}^f = E\epsilon^2/(1 - \nu)$ (where E is the Young's modulus). For the substrate, the corresponding base state is stress-free, with $\bar{u}_i^s = \bar{u}_{ij}^s = \bar{\sigma}_{ij}^s = 0$.

The elastic properties at higher orders can be obtained by substituting the expansions (9) and (10) into Eqs. (5)–(8). In Fourier space the Navier's equations (5) can be rewritten as

$$(1 - 2\nu)(\partial_z^2 - q^2)\hat{u}_j^{(\xi)} + iq_j \left[iq_x \hat{u}_x^{(\xi)} + iq_y \hat{u}_y^{(\xi)} + \partial_z \hat{u}_z^{(\xi)} \right] = 0, \quad \text{for } j = x, y, \quad (11)$$

$$(1 - 2\nu)(\partial_z^2 - q^2)\hat{u}_z^{(\xi)} + \partial_z \left[iq_x \hat{u}_x^{(\xi)} + iq_y \hat{u}_y^{(\xi)} + \partial_z \hat{u}_z^{(\xi)} \right] = 0, \quad (12)$$

for ξ th order expansion ($\xi = 1, 2, 3, \dots$). The corresponding general solutions have the same format as that obtained in Ref. 6 for 1st order equations, which read

$$\hat{u}_i^{(\xi)f} = \begin{bmatrix} \alpha_x^{(\xi)} \\ \alpha_y^{(\xi)} \\ \alpha_z^{(\xi)} \end{bmatrix} \cosh(qz) + \begin{bmatrix} \beta_x^{(\xi)} \\ \beta_y^{(\xi)} \\ \beta_z^{(\xi)} \end{bmatrix} \sinh(qz) - \begin{bmatrix} C^{(\xi)} iq_x/q \\ C^{(\xi)} iq_y/q \\ D^{(\xi)} \end{bmatrix} z \sinh(qz) - \begin{bmatrix} D^{(\xi)} iq_x/q \\ D^{(\xi)} iq_y/q \\ C^{(\xi)} \end{bmatrix} z \cosh(qz) \quad (13)$$

for the film, and

$$\hat{u}_i^{(\xi)s} = \begin{bmatrix} \alpha_x^{(\xi)} \\ \alpha_y^{(\xi)} \\ \alpha_z^{(\xi)} \end{bmatrix} e^{qz} - \begin{bmatrix} iq_x/q \\ iq_y/q \\ 1 \end{bmatrix} B^{(\xi)} z e^{qz} \quad (14)$$

for the substrate after using the boundary conditions (7) and (8) at the film-substrate interface and inside the substrate. The coefficients $\alpha_i^{(\xi)}$, $\beta_i^{(\xi)}$, $C^{(\xi)}$, $D^{(\xi)}$, and $B^{(\xi)}$ in Eqs. (13) and (14) are determined via the expansion of boundary conditions (6)–(7) in orders of perturbation \hat{h} . Note that the 1st order solution has been known with the use of linearized boundary conditions^{6,10}, with the perturbed elastic energy density being given by

$$\hat{\mathcal{E}}^{(1)f} = -\frac{2E(1 + \nu)}{1 - \nu} \epsilon^2 q \hat{h}(\mathbf{q}). \quad (15)$$

For the 2nd order expansion of the boundary conditions, at the top surface of the film, $z = h$, Eq. (6) can be written as

$$-\sum_{\mathbf{q}'} i(q_x - q'_x) \hat{\sigma}_{jx}^{(1)f}(\mathbf{q}') \hat{h}(\mathbf{q} - \mathbf{q}') - \sum_{\mathbf{q}'} i(q_y - q'_y) \hat{\sigma}_{jy}^{(1)f}(\mathbf{q}') \hat{h}(\mathbf{q} - \mathbf{q}') + \hat{\sigma}_{jz}^{(2)f}(\mathbf{q}) = 0, \quad (16)$$

while the continuity of stress at the film-substrate interface $z = 0$ (i.e., Eq. (7)) yields

$$\hat{\sigma}_{jz}^{(2)f}(\mathbf{q}) = \hat{\sigma}_{jz}^{(2)s}(\mathbf{q}), \quad (17)$$

with $j = x, y, z$. Substituting Eqs. (13) and (14) to these boundary conditions (16) and (17), the second order coefficients of the solution can be obtained as follows:

$$\begin{aligned} q\alpha_z^{(2)} = q\beta_z^{(2)} &= -e^{-q\bar{h}} \left[\frac{a_1^{(2)} q_x + b_1^{(2)} q_y}{2\mu q} (1 - 2\nu + q\bar{h}) - \frac{c_1^{(2)}}{2\mu} (2 - 2\nu + q\bar{h}) \right], \\ iq_x \alpha_x^{(2)} + iq_y \alpha_y^{(2)} = iq_x \beta_x^{(2)} + iq_y \beta_y^{(2)} &= e^{-q\bar{h}} \left[\frac{a_1^{(2)} q_x + b_1^{(2)} q_y}{2\mu q} (q\bar{h} - 2 + 2\nu) + \frac{c_1^{(2)}}{2\mu} (1 - 2\nu + q\bar{h}) \right], \\ C^{(2)} = D^{(2)} = B^{(2)} &= e^{-q\bar{h}} \left[-\frac{a_1^{(2)} q_x + b_1^{(2)} q_y}{2\mu q} + \frac{c_1^{(2)}}{2\mu} \right], \end{aligned} \quad (18)$$

where

$$\begin{aligned} a_1^{(2)}q_x + b_1^{(2)}q_y &= \sum_{\mathbf{q}'} \hat{h}(\mathbf{q} - \mathbf{q}') \hat{h}(\mathbf{q}') \left\{ \frac{2E\epsilon}{q'(1-\nu)} [q_x(q_x - q'_x)(q_x'^2 + \nu q_y'^2) + q_y(q_y - q'_y)(q_y'^2 + \nu q_x'^2)] \right. \\ &\quad \left. + 2E\epsilon \frac{q'_x q'_y}{q'} [q_x(q_y - q'_y) + q_y(q_x - q'_x)] \right\}, \end{aligned} \quad (19)$$

and

$$c_1^{(2)} = \sum_{\mathbf{q}'} \hat{h}(\mathbf{q} - \mathbf{q}') \hat{h}(\mathbf{q}') \frac{E\epsilon}{1-\nu} [q'_x(q_x - q'_x) + q'_y(q_y - q'_y)]. \quad (20)$$

Based on the above solution, we can determine the second order elastic energy density, i.e.,

$$\begin{aligned} \hat{\mathcal{E}}^{(2)f} &= \sum_{\mathbf{q}'} \left[\frac{1+\nu}{2E} \hat{\sigma}_{ij}^{(1)f}(\mathbf{q}') \hat{\sigma}_{ij}^{(1)f}(\mathbf{q} - \mathbf{q}') - \frac{\nu}{2E} \hat{\sigma}_{il}^{(1)f}(\mathbf{q}) \hat{\sigma}_{il}^{(1)f}(\mathbf{q} - \mathbf{q}') \right] \\ &\quad + \frac{E\epsilon}{1-\nu} \left[(1-\nu) \frac{a_1^{(2)}q_x + b_1^{(2)}q_y}{\mu q} - (1-2\nu) \frac{c_1^{(2)}}{2\mu} \right], \end{aligned} \quad (21)$$

where the expressions of 1st-order stress tensor $\hat{\sigma}_{ij}^{(1)f}$ at the top surface are given in the appendix [see Eqs. (A.11)–(A.16)]. The 2nd-order stress tensor can be also calculated, with results shown in Eqs. (A.5)–(A.10) of the appendix.

We then derive the nonlinear evolution equation for film surface morphology from Eq. (2), using the results of perturbed elastic energy density given in Eqs. (15) and (21). All the terms in the dynamic equation (2) are expanded up to second order of surface perturbation \hat{h} , except for $W(h)$ for which the full nonlinear wetting potential form Eq. (3) is used. For the surface energy term $\gamma\kappa$, noting that the surface curvature $\kappa = -\nabla \cdot [\nabla h / \sqrt{1 + |\nabla h|^2}]$, we have $\gamma\kappa \sim -\gamma\nabla^2 h + \mathcal{O}(\hat{h}^3)$ and hence only need to keep the linear order term in the 2nd-order approximation considered here. To further simplify the calculation, we choose a length scale $l = \gamma/\mathcal{E}_0$ and a time scale $\tau = l^4/\gamma\Gamma_h$, where the characteristic strain energy density $\mathcal{E}_0 = 2E\epsilon_0^2(1+\nu)/(1-\nu)$ with ϵ_0 a reference misfit value. The resulting nondimensional dynamic equation for the perturbed surface profile $\hat{h}(\mathbf{q}, t)$ is given by

$$\frac{\partial \hat{h}}{\partial t} = (-q^4 + \epsilon^{*2} q^3) \hat{h} - q^2 \mathcal{W}_{\mathbf{q}} - \epsilon^{*2} \sum_{\mathbf{q}'} \hat{h}(\mathbf{q}') \hat{h}(\mathbf{q} - \mathbf{q}') \Lambda(\mathbf{q}, \mathbf{q}'), \quad (22)$$

where $\mathcal{W}_{\mathbf{q}}$ is the Fourier transform of the rescaled wetting potential $W(h)/\mathcal{E}_0$, $\epsilon^* = \epsilon/\epsilon_0$, and

$$\begin{aligned} \Lambda(\mathbf{q}, \mathbf{q}') &= q^2 \left[(1-\nu) \frac{[\mathbf{q}' \cdot (\mathbf{q} - \mathbf{q}')]^2}{q' |\mathbf{q} - \mathbf{q}'|} - \mathbf{q}' \cdot (\mathbf{q} - \mathbf{q}') + \nu q' |\mathbf{q} - \mathbf{q}'| \right] \\ &\quad + \frac{2q}{q'} \left\{ q_x(q_x - q'_x)(q_x'^2 + \nu q_y'^2) + q_y(q_y - q'_y)(q_y'^2 + \nu q_x'^2) + (1-\nu) q'_x q'_y [q_x(q_y - q'_y) + q_y(q_x - q'_x)] \right\}. \end{aligned} \quad (23)$$

In Eq. (22), the first term of the right-hand-side is the combination of the surface energy contribution and the 1st order elastic energy density $\hat{\mathcal{E}}^{(1)f}$, consistent with the previous linear-order results^{6,31,34}. The last term is from the 2nd-order perturbation result of the elastic energy density, i.e., Eq. (21) for $\hat{\mathcal{E}}^{(2)f}$. It would be straightforward, although with more complicated processes, to extend the above approach to incorporate higher-order contributions, based on the perturbed analysis of system elasticity given in Eqs. (9)–(14). That is, to obtain the n th-order elastic results, we can first express the n th-order expansion of the boundary conditions in terms of ξ th-order ($\xi = 1, 2, \dots, n-1, n$) stress tensors [similar to the expression in Eq. (16)], and use it to calculate the n th-order solution of the displacement field given in Eq. (13); The corresponding film elastic properties can then be derived, particularly the n th-order elastic energy density $\hat{\mathcal{E}}^{(n)f}$ at the film surface which can be expressed as a function of ξ th-order ($\xi = 1, 2, \dots, n-1$) elastic quantities that are already known. We have applied this recursive method to third-order calculations, with results of elastic energy density $\hat{\mathcal{E}}^{(3)f}$ shown in the appendix. The corresponding higher-order evolution equation can be obtained via adding term $-q^2 \hat{\mathcal{E}}^{(3)f}$ to Eq. (22).

IV. LINEAR STABILITY ANALYSIS

In the following studies of film evolution and strained island dynamics, we focus on Eq. (22) with 2nd-order elastic properties. Here we first perform a linear stability analysis of Eq. (22) to determine the conditions of morphological

instability of the system; such conditions are needed for the nonlinear calculations given in Sec. V and Sec. VI. Following the standard procedure, we assume an exponential growth $\hat{h} = \hat{h}_0 \exp(\sigma_h t)$ at early time, and apply it to the linearized evolution equation of \hat{h} . The characteristic equation for the perturbation growth rate σ_h is then given by

$$\sigma_h = -q^4 + q^3 \epsilon^{*2} - q^2 a, \quad (24)$$

where $a = (w^*/h_{ml}^*)(x + \alpha_w)x^{-\alpha_w-1}e^{-x}$, $x = \bar{h}/h_{ml}$, $w^* = w/\mathcal{E}_0$, and $h_{ml}^* = h_{ml}/l$. From the above dispersion relation we can identify the condition for the occurrence of film morphological instability, which is given by $\epsilon^{*4} \geq 4a$ or equivalently,

$$\frac{e^x x^{\alpha_w+1}}{x + \alpha_w} \geq \frac{4w^*}{\epsilon^{*4} h_{ml}^*}. \quad (25)$$

The corresponding characteristic wave number of film instability (for the fastest instability growth mode) can be written as

$$q_{\max} = \frac{3}{8} \left[\epsilon^{*2} + \sqrt{\epsilon^{*4} - \frac{32}{9}a} \right]. \quad (26)$$

Eq. (25) is used to identify the parameters in our numerical simulations shown below, for which the initial film instability and hence the appearance of nonplanar surface morphology or islands are required. Note that for given film conditions such as misfit strain ϵ and wetting parameters, Eq. (25) indicates that due to the film-substrate wetting effect (with $\alpha_w > 0$), the morphological instability and surface nanostructures will develop only for thick enough films, with the critical thickness \bar{h}_c determined by Eq. (25), i.e., $e^{x_c} x_c^{\alpha_w+1}/(x_c + \alpha_w) = 4w^*/\epsilon^{*4} h_{ml}^*$ (where $x_c = \bar{h}_c/h_{ml}$); the value of \bar{h}_c increases with smaller film-substrate misfit strain. Also, the characteristic size (or wavelength $\lambda = 2\pi/q_{\max}$) of surface structures at the initial stage will decrease with the increasing average film thickness \bar{h} , as can be obtained from Eq. (26).

V. EFFECTS OF WETTING POTENTIAL

To validate our model system and the nonlinear dynamic equation (22) derived above, we first examine the effect of wetting potential on film evolution and compare it to the well-known results of cusp formation obtained from previous full elasticity calculations^{23,25}. Since Eq. (22) is already presented in Fourier space, in our numerical simulations we directly use the spectral method with periodic boundary conditions along the lateral x and y directions, and also an exponential propagation algorithm for time integration⁴⁶. This allows us to use large enough time steps (up to $\Delta t = 1$ in most results shown below, except for the study of groove/cusp formation for which $\Delta t = 0.01$ is used). For rescaling parameters that are associated with the nondimensional equation (22), the reference misfit $\epsilon_0 = 3\%$ is chosen, and thus the length scale can be estimated as $l \simeq 5.5$ nm if using the material parameters of Ge/Si system. For simplicity, in this work we focus on the case of nongrowing films with deposition rate $v = 0$ and simulate the annealing process of film evolution.

As found first by Yang and Srolovitz²³ and later in various numerical studies of 2D^{25,28} and 3D^{30,33} systems via solving either the full elasticity problem or the reduced nonlinear evolution equations, deep grooves or cusps will form in stressed solid systems without the incorporation of wetting effect. This is well reproduced in our numerical results of Eq. (22), as shown in Fig. 1 for 3% misfit films with $\nu = 1/3$ and initial film thickness $h_0 = 0$. Two types of initial conditions are used: (1) a small random disturbance of a planar film of thickness h_0 , with results of a 128×128 system presented in Fig. 1 (a) and (b), and (2) a weakly perturbed film with doubly-periodic sinusoidal surface profile $h = h_0 + A_0[\cos(q_{x0}x) + \cos(q_{y0}y)]$, as given in panels (c) and (d) of Fig. 1 for a $\lambda_{x0} \times \lambda_{y0}$ system (where $\lambda_{x0} = 2\pi/q_{x0}$ and $\lambda_{y0} = 2\pi/q_{y0}$). For condition (2) the initial perturbed amplitude is set as $A_0 = 0.01$, and a perturbed wavevector $q_{x0} = q_{y0} = 3/4\sqrt{2}$ is chosen, corresponding to the wave number of the most linearly unstable mode determined by Eq. (26). In both cases the formation of singular cusps or deep grooves and their rapid growth have been found during the film evolution, as evidenced by the 3D morphological profiles given in Fig. 1 (a) and (c), and also from the results of time-evolving 2D cross-section profiles shown in (b) and (d) which are consistent with the previous 2D results of Spencer and Meiron²⁵ and Xiang and E²⁸.

To incorporate the wetting effect, in our calculations we use a pseudospectral method; that is, we first evaluate the wetting potential $W(h)$ from Eq. (3) in real space and then obtain its Fourier component $\mathcal{W}_{\mathbf{q}}$ as used in the dynamic equation (22). As expected, the cusp/groove singularity is completely suppressed by the film-substrate

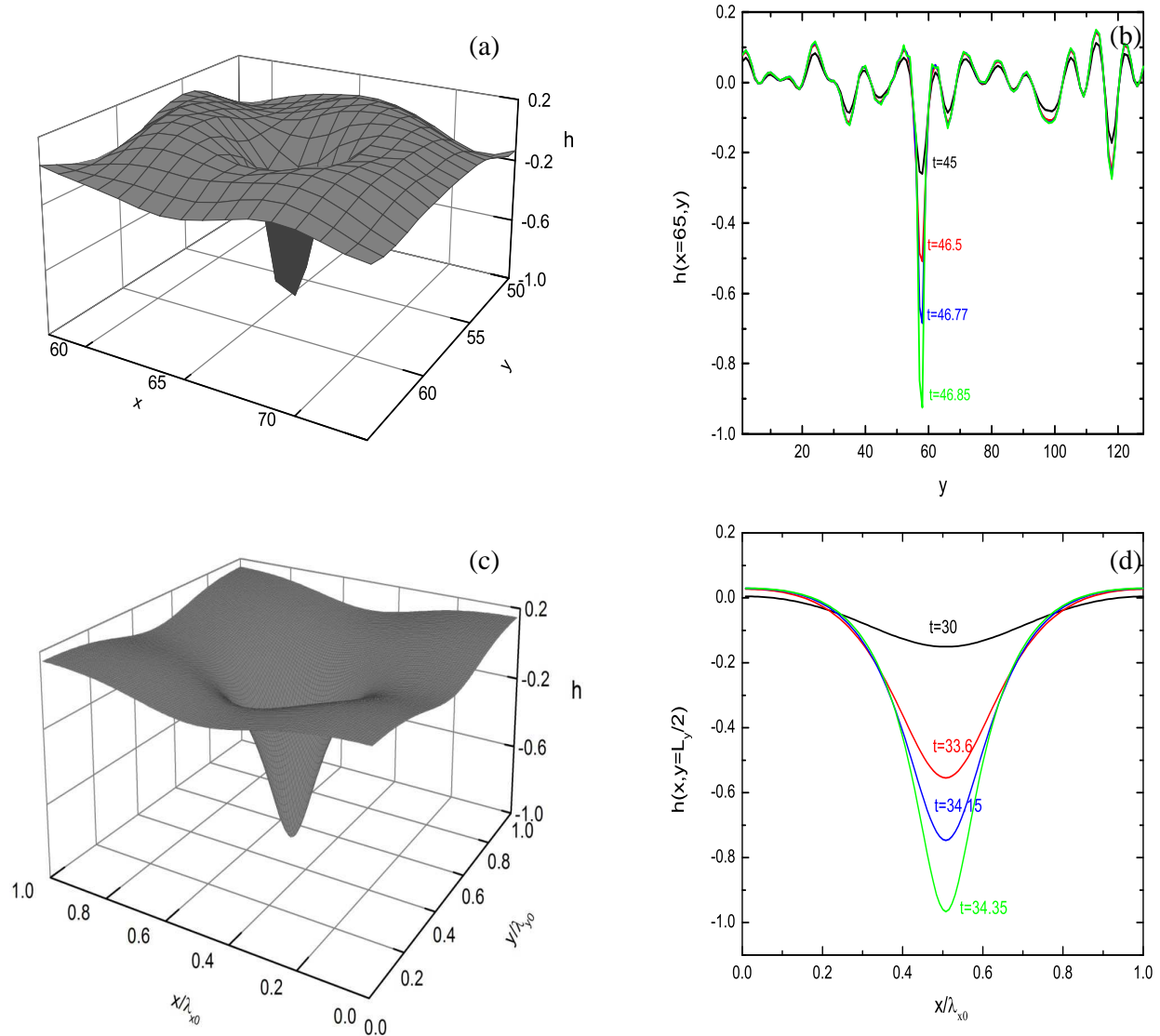


FIG. 1: Surface morphologies of 3% strained films, as obtained from numerical simulations without the wetting effect. The simulations start either from small random initial perturbation of a planar film [(a) and (b)] or from a doubly-periodic surface profile with wavevector $q_{x0} = q_{y0} = 3/4\sqrt{2}$ and amplitude $A_0 = 0.01$ [(c) and (d)]. Both 3D morphologies, (a) at $t = 46.77$ for a portion of a 128×128 system and (c) at $t = 34.35$ for system size $\lambda_{x0} \times \lambda_{y0}$, and also time evolution of 2D cross-section profiles are shown.

wetting interaction, and arrays of strained islands or quantum dots will form and grow. This has been verified by our numerical results shown in Fig. 2, where we have used the parameters of $\epsilon = 3\%$, $h_0 = 0.41$, $h_{ml}^* = 0.3$, $\alpha_w = 2$, $w^* = 0.08$ or 0.2 , and simulation time step $\Delta t = 1$. However, another type of growth instability would occur when the strength of wetting interaction is not strong enough (e.g., $w^* = 0.08$ in Fig. 2), showing as the rapid increase of island heights beyond initial time stage and then the blow-up of numerical solution at late times. Such instability with unbound growth of island height is absent for stronger wetting effect, such as the effect of $w^* = 0.2$ shown in Fig. 2(a) which gives the stabilization and saturation of island evolution. This can be understood from the fact that the wetting interaction tends to prevent the depletion of the film-substrate wetting layer and hence suppress the mass transport from the valley of an island to its top, leading to the constraint of island height as a result of mass conservation. Such effect would increase with the strength of wetting interaction, as can be seen from the results given

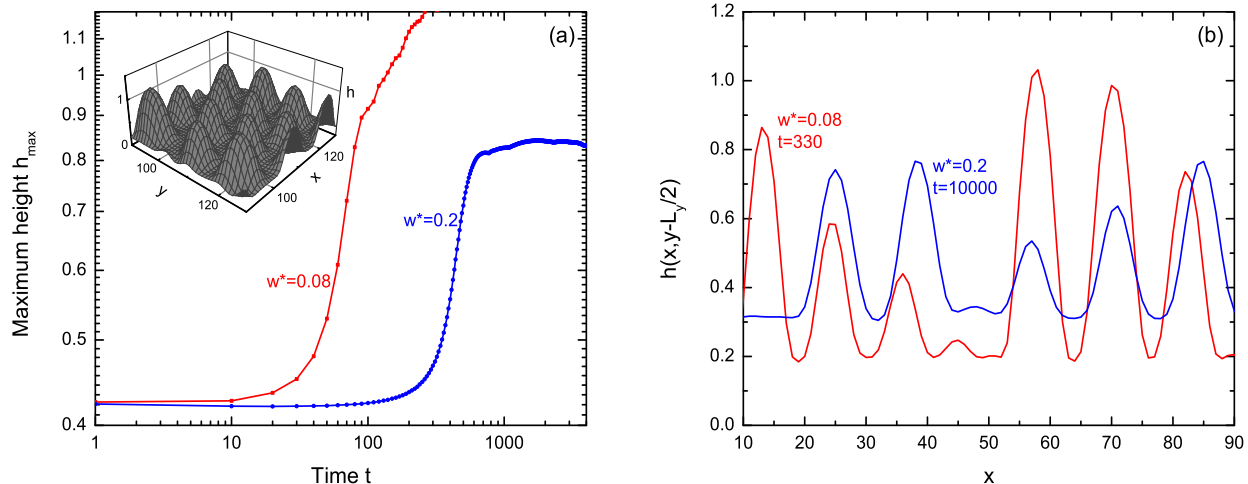


FIG. 2: Time evolution of 3% strained films with different wetting strength $w^* = 0.08$ and 0.2 . (a) Evolution of maximum surface height, with a 3D island morphology for $w^* = 0.08$ at $t = 330$ shown in the inset; (b) 2D cross-section profiles at $y = L_y/2$ for $w^* = 0.08$ at $t = 330$ and $w^* = 0.2$ at $t = 10000$.

in Fig. 2(b): thicker film layers between surface islands and shallower valleys are found for larger wetting strength w^* , as a result of stronger suppression on the valley-to-peak diffusion process.

VI. RESULTS OF NONLINEAR EVOLUTION

To examine the detailed evolution of strained film morphology more systematically, we have conducted numerical simulations of the full dynamic equation (22) for different small film-substrate misfit strains $\epsilon = 2\%$, 2.5% , and 3% (in such weak strain limit the continuum elasticity approach can be well applied, as shown in most recent studies⁴³). The parameters for the wetting potential are chosen as $h_{ml}^* = 0.3$, $\alpha_w = 2$, and $w^* = 0.2$, with all other parameters the same as those given in Sec. V. In our simulations we have used 3 different system sizes $L_x \times L_y$ for each parameter set, including the lateral dimensions of 128×128 , 256×256 , and 512×512 , to examine any possible artifacts of finite size effects. A numerical grid spacing $\Delta x = \Delta y = 1$ is adopted, and the integration time step is chosen as $\Delta t = 1$. The quantitative results given below have been averaged over 20 independent runs for system sizes 128×128 and 256×256 , and 10 runs for 512×512 . Also, each simulation starts with a rescaled initial film thickness of $h_0 = 0.67$ for misfit strain $\epsilon = 2\%$, $h_0 = 0.5$ for $\epsilon = 2.5\%$, and $h_0 = 0.41$ for $\epsilon = 3\%$, all of which are within the corresponding instability parameter region for each misfit as determined by Eq. (25).

Typical simulation results of film evolution and the formation and dynamics of quantum dot arrays are illustrated in Fig. 3, for 2.5% mismatch between the film and substrate. At the beginning stage surface undulations occur due to film morphological instability determined in Eq. (25), leading to the formation of strained surface islands or quantum dots as shown in Fig. 3(a). Note that at different surface locations, islands will form and grow gradually at different rates due to the nonlinear effects of elastic interaction. Island coarsening occurs at the next stage, showing as the growth of some quantum dots at the expense of other shrinking ones and hence the decrease of island density on the film surface. This can be seen more clearly in the corresponding 2D top-view images of Figs. 3(d)–(f), which give the comparison of island distribution between times $t = 1000$, 2000 , and 10^4 . Such coarsening process becomes much slower as time increases, and the system would approach an asymptotic state with steady arrays of strained quantum dots. As expected, this late-time state of film surface structures highly depends on the value of film-substrate misfit strain, with an increase of island density and a decrease of island spacing for larger misfits. This has been confirmed in our results of 2% and 3% films given in Fig. 4, as compared to the 2.5% film shown in Figs. 3(c) and 3(f). In our simulations no long-range spatial order can be found for quantum dot arrays, even at the late-time stage, agreeing with the observation of most experimental and theoretical studies.

To quantify the above results, we have analyzed the film surface morphology through various time-dependent parameters, including the structure factor of surface height, its moments, the maximum height of surface profile, and

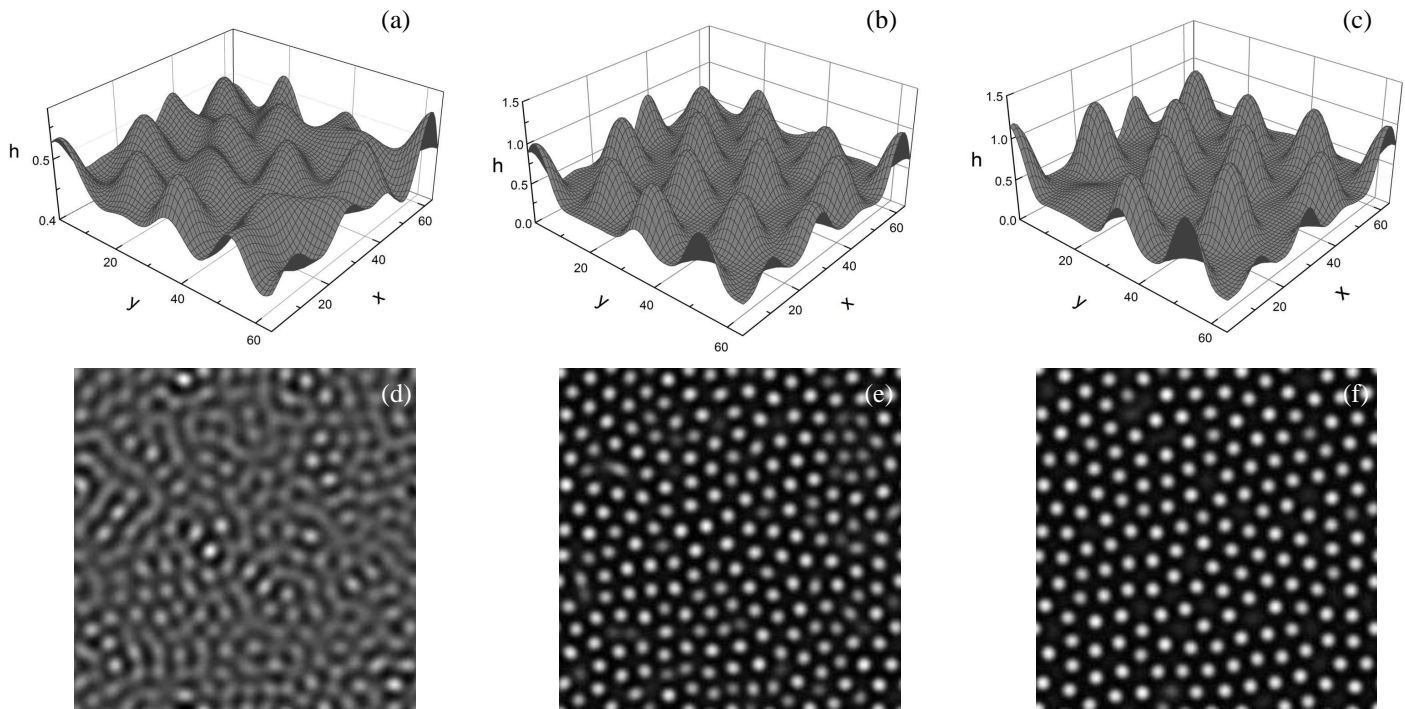


FIG. 3: Morphological profiles of a 2.5% strained film, at simulation times $t = 1000$ [(a) and (d)], 2000 [(b) and (e)], and 10000 [(c) and (f)]. A fraction of 3D morphologies in a 256×256 system is given in panels (a)–(c), while the corresponding 2D gray scale top-view images of the full system size are shown in (d)–(f).

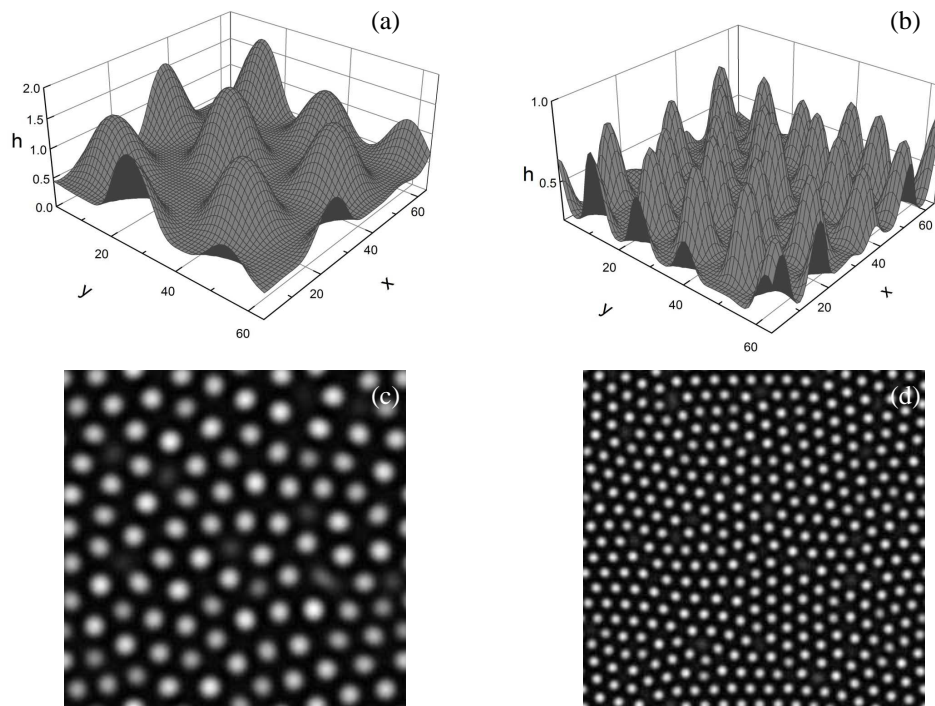


FIG. 4: Morphological profiles of (a) 2% and (b) 3% strained films at late time stage of $t = 10000$. Only a portion of the 256×256 system is shown in the 3D images of (a) and (b). The corresponding 2D top-view images of the full system size are given in (c) and (d).

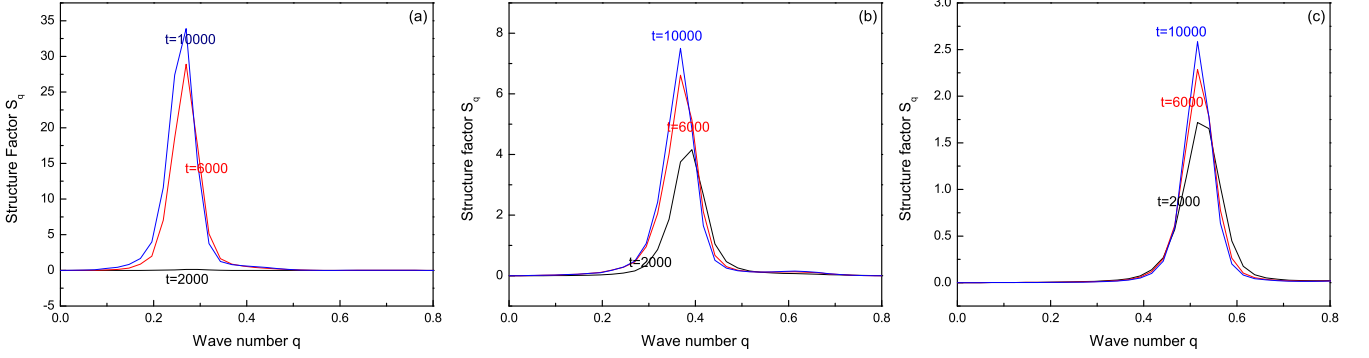


FIG. 5: Structure factor of the surface height as a function of wave number q , for different misfits (a) $\epsilon = 2\%$, (b) $\epsilon = 2.5\%$, and (c) $\epsilon = 3\%$, system size 256×256 , and times $t = 2000, 6000$, and 10000 .

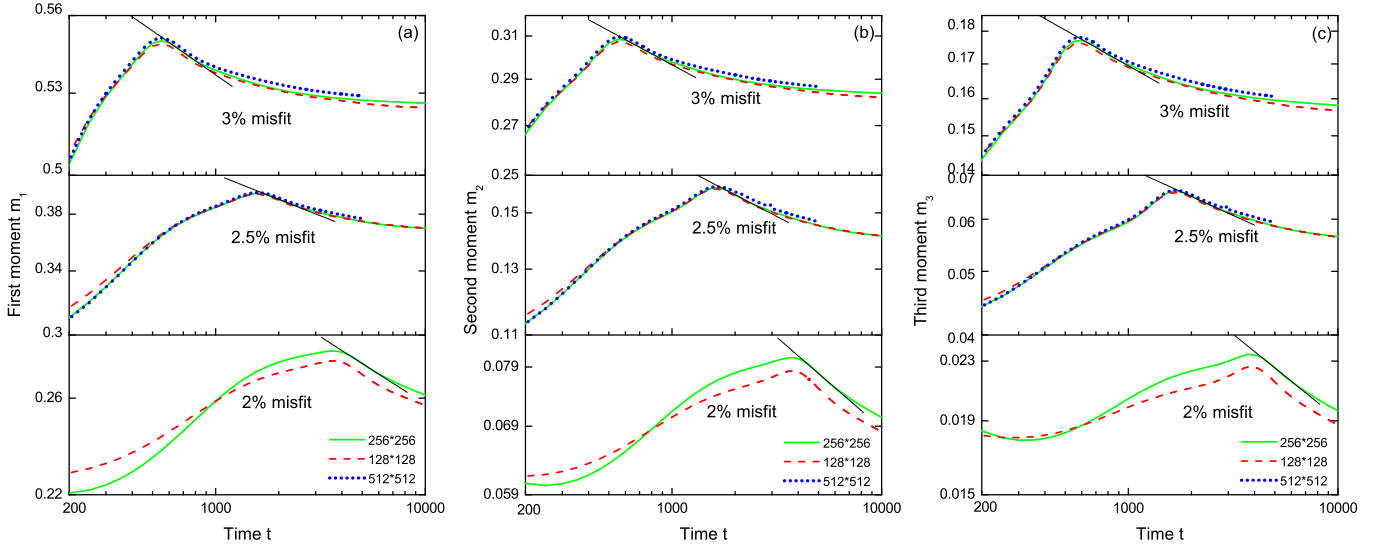


FIG. 6: Time evolution of the three moments of structure factor: (a) m_1 , (b) m_2 , and (c) m_3 , for misfit strains $\epsilon = 2\%$, 2.5% , and 3% . The solid lines represent the simulation results of grid size 256×256 , whereas the dashed and dotted lines represent the results for grid sizes 128×128 and 512×512 respectively. Power law fittings (i.e., the thin lines) at the beginning of coarsening stage for the 256×256 system are also shown.

the surface roughness, as shown in Figs. 5–8 with results of different system sizes presented. The structure factor is defined as $S(q, t) = \langle |\hat{h}(\mathbf{q}, t)|^2 \rangle_{\hat{q}}$, with a circular average over orientation \hat{q} of the wave number. Typical results of $S(q, t)$ are given in Fig. 5, for different misfit strains of 2% , 2.5% , and 3% . As the misfit increases, the wave number related to the peak location of the structure factor becomes larger, corresponding to smaller island spacing and also higher quantum dot density as already seen in Figs. 4(c), 3(f), and 4(d). Also, for smaller misfit strain larger time is needed for the initial formation of islands (if we compare the $t = 2000$ curves in Figs. 5(a)–(c)), consistent with the result of σ_h in the linear stability analysis.

Details of the time evolution of quantum dot islands can be characterized by the calculation of various moments of the structure factor. The n th moment of $S(q, t)$ is defined as

$$m_n(t) = \frac{\int dq q^n S(q, t)}{\int dq S(q, t)}, \quad (27)$$

which yields the information of the characteristic size and spatial scale of surface structures⁴⁷. We have calculated the

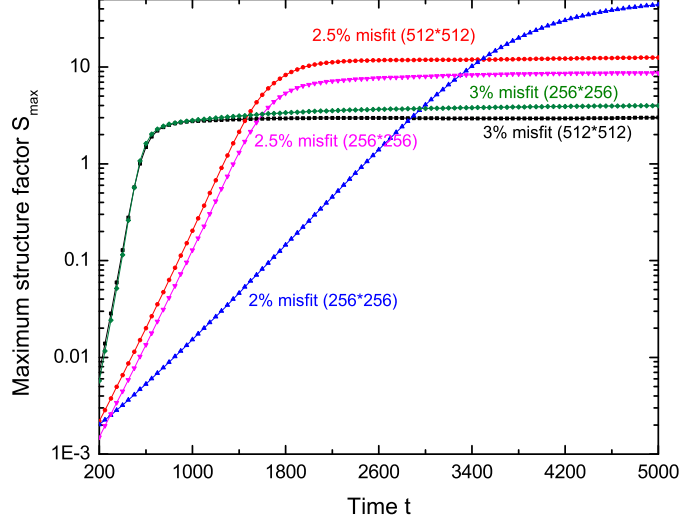


FIG. 7: Time evolution of the maximum value of structure factor, for misfits $\epsilon = 2\%$, 2.5% , and 3% . Results for different system sizes 256×256 and 512×512 are shown for comparison.

first three moments of $S(q, t)$, with time evolution results for three different misfits given in Figs. 6(a) (for m_1), 6(b) (for m_2), and 6(c) (for m_3). Three characteristic regimes of film evolution can be identified in each simulation: the process of surface instability development and island formation at early times, coarsening of these strained islands at intermediate stage, and an asymptotic stage of island saturation at late times. The first two stages can be distinguished clearly in the results of moments shown in Fig. 6, as separated by the turning point (i.e., maximum of m_n) of the time evolution curve for each moment. The increase of m_n at the first time stage is due to the continuous appearance of new islands at various times as observed in our simulations, and thus the decrease of average island spacing. The time range of this early stage of island formation is longer for smaller misfit strain, as a result of overall smaller instability growth rate [see Eqs. (24)–(26)]. This has been verified in Fig. 6, via comparing the three panels of misfits 3% , 2.5% , and 2% (from top to bottom) for results of each moment.

Once most islands have formed (i.e., when the moments m_n reach maximum values), they start to coarsen so that the average distance between islands increases, leading to the decrease of m_n . A power-law behavior of coarsening, $m_n(t) \sim t^{-\beta_n}$, can be obtained, but such behavior is limited to a transient time range at the beginning of the coarsening stage. As shown in Fig. 6, this time range is smaller for larger film-substrate misfit strain ϵ , with faster crossover to a saturated state. Also, slower coarsening rate has been found for larger misfit, corresponding to smaller coarsening exponents β_n which are identified as (for system size 256×256): For $\epsilon = 2\%$, $\beta_1 = 0.1010 \pm 0.0008$, $\beta_2 = 0.181 \pm 0.002$, and $\beta_3 = 0.235 \pm 0.003$; For $\epsilon = 2.5\%$, $\beta_1 = 0.0702 \pm 0.0007$, $\beta_2 = 0.120 \pm 0.002$, and $\beta_3 = 0.145 \pm 0.004$; For $\epsilon = 3\%$, $\beta_1 = 0.0449 \pm 0.0009$, $\beta_2 = 0.076 \pm 0.003$, and $\beta_3 = 0.090 \pm 0.006$. Note that if the structure factor is assumed to obey a simple dynamic scaling behavior due to coarsening, one would usually expect that $m_n(t) \sim t^{-n\beta_1}$; i.e., $\beta_n = n\beta_1$. However, the above results of coarsening exponents in the intermediate time range for all different misfit strains do not support this assumption, and we cannot identify a simple format of scaling for the structure factor. This might be attributed to the complex relaxation of strain energy in the film and the nonlinear elastic interaction between surface islands [see e.g., Eq. (23)] which are more complicated than that revealed by simple scaling.

These two regimes of island formation and coarsening are also illustrated in our numerical results for the maximum value of the structure factor S_{\max} (Fig. 7), the maximum surface height h_{\max} (Fig. 8), and the surface roughness $r(t) = \langle (h - \bar{h})^2 \rangle^{1/2}$ (Fig. 9). The growth of all three quantities can be observed during the first stage of instability growth and island formation, which corresponds to the same initial time range as the m_n results shown in Fig. 6. Both S_{\max} and the roughness $r(t)$ grow exponentially with time at this stage, consistent with the behavior of linear instability analyzed in Sec. III. However, at later times during the coarsening process, these quantities show rather slow growth and an approach to saturation, even for h_{\max} . Such phenomenon of surface roughness saturation has been obtained in a recent study of a nonlinear evolution equation³³, but not in other studies using different evolution equations (which instead observed power-law growth)^{34,35}. The limited growth of maximum surface height given in Fig. 8 during island coarsening has not been reported in those previous studies, which usually showed a faster growth

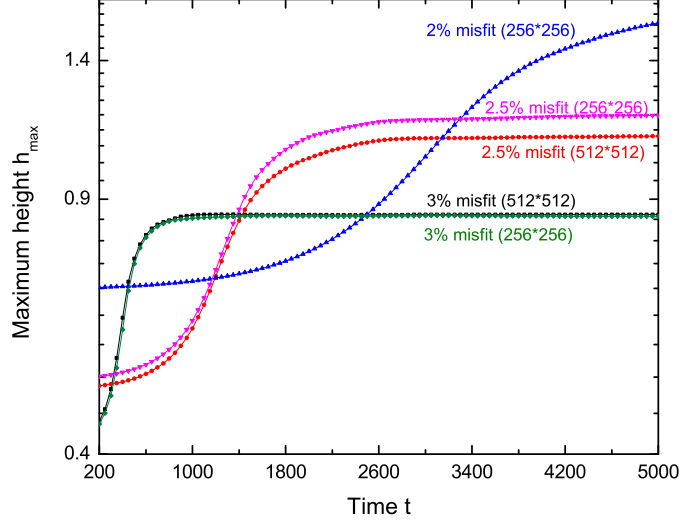


FIG. 8: Time evolution of maximum surface height for misfits $\epsilon = 2\%$, 2.5% , and 3% and system sizes 256×256 and 512×512 .

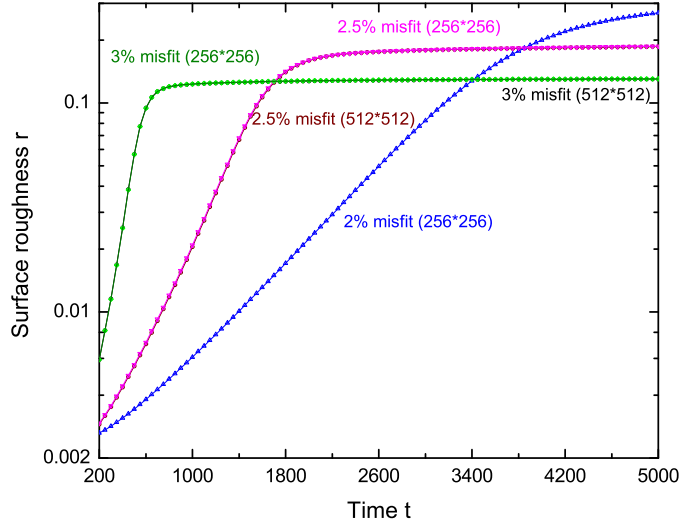


FIG. 9: Time evolution of surface roughness for various misfits $\epsilon = 2\%$, 2.5% and 3% . Note that for each misfit, results of different system sizes 256×256 and 512×512 almost overlap with each other.

of h_{\max} such as a power-law behavior³⁴.

Our simulation results also indicate a crossover from the island coarsening regime to an asymptotic state of steady quantum dot arrays, showing as saturated values of S_{\max} , h_{\max} , and $r(t)$ (see the 2.5% and 3% results in Figs. 7–9), and more clearly, the saturation of m_n given in Fig. 6. Such crossover can be identified through the slowing of the m_n decay after the transient of power-law-type coarsening, and occurs earlier for larger misfit strain. To exclude any artifacts from finite size effects, we have tested our simulations for different system sizes ranging from 128×128 to 512×512 , with qualitatively similar results obtained. This phenomenon of the slowing and saturation of coarsening process has been found in some experiments of Ge/Si systems^{16,17,19,22} and also in some modeling and simulation results based on either direct solution of system elasticity^{26,32} or reduced film evolution equations^{33,36}; however, no

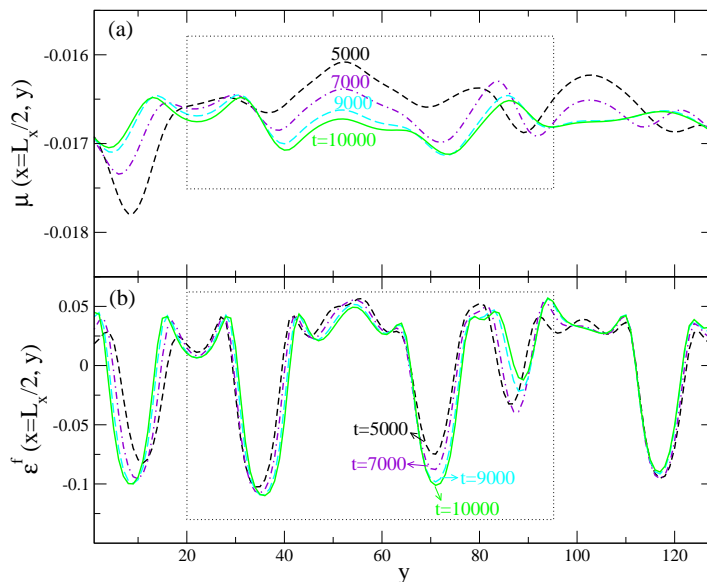


FIG. 10: Cross-section profiles of (a) surface chemical potential μ and (b) elastic energy density \mathcal{E}^f , for misfit $\epsilon = 2.5\%$ and different times $t = 5000, 7000, 9000,$ and 10000 . The boxed region will be further studied in Fig. 11.

sign of coarsening termination in annealing films has been shown in some other experimental²⁰ and theoretical^{29,34,35} work. Also, the effect of different misfit strains on island coarsening and saturation, which is shown important from our results here, has not been addressed in most previous studies. Our results given above suggest that much longer times are needed to observe the slowing or cessation of island coarsening for smaller misfits, which could be useful for addressing the discrepancy of experimental observation: E.g., the suppression or saturation of quantum dot growth can be found at relatively short annealing times for Ge/Si(001) system with large misfit ($\sim 4\%$)^{16,17,19}, while it is more difficult to observe in SiGe/Si(001) experiments with weak misfit strain ($< 1\%$)²⁰.

VII. DISCUSSION

To understand the mechanisms underlying the saturation phenomenon given above, it would be helpful to examine the effects of all contributed terms in the evolution equation (22). As already discussed in Sec. V, the wetting potential plays a crucial role on the stabilization of surface morphology via limiting the valley-to-peak mass transport and thus the growth of island height. Similar mechanism is expected during island coarsening, and the stabilization effect of wetting potential should be also important for the island size saturation. On the other hand, the dynamics of coarsening involves the redistribution of mass between different islands, a process that cannot be constrained by the wetting effect as long as the wetting layer is not depleted. Thus additional factor(s) must be in play to account for the island saturation and stabilization process.

To further illustrate the saturating process, we show in Fig. 10 the time-varying profiles of the chemical potential $\mu = \gamma\kappa + W + \mathcal{E}^f$ at the film surface and also its corresponding elastic contribution \mathcal{E}^f (i.e., the surface elastic energy density). For simplicity, only the cross-section results at $x = L_x/2$ are presented, for an example of 2.5% misfit film. Smaller spatial variations of chemical potential μ along the film surface are obtained at later times [note the very small vertical scale in Fig. 10(a)], indicating an approach to an asymptotic saturated state. This is consistent with the results given in Figs. 6–9 for various morphological properties, and also with the evolution profiles of elastic energy density \mathcal{E}^f given in Fig. 10(b). Furthermore, in Fig. 11 we examine the detailed mechanisms of such saturation through identifying the time evolution of various components of chemical potential, including the surface-energy contribution $\gamma\kappa$ and the first and second order elastic energy densities $\mathcal{E}^{(1)f}$ and $\mathcal{E}^{(2)f}$. We focus on a small region of 4 islands [see Fig. 11(a)], representing 3 scenarios of quantum dot evolution: (1) large islands that are growing and saturating, (2) small islands that are shrinking [see the middle island in Fig. 11(a)], and (3) islands that are migrating (see the one at the right corner). As expected from previous analysis⁶, for an undulated surface (i.e., in the region of surface islands), the strain energy is concentrated at surface valleys but released at peaks; the resulting surface elastic energy density gradient would drive the diffusion process from the valleys to peaks and thus the growth of surface islands. On the other hand, this morphological destabilization process is competed by the stabilization effect

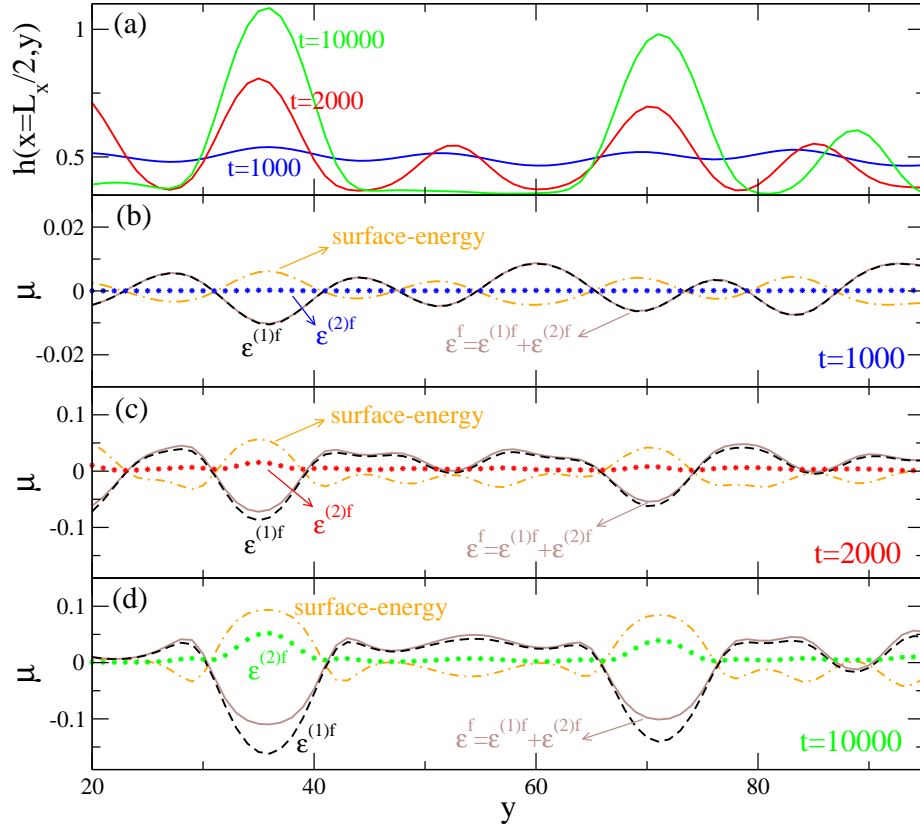


FIG. 11: Cross-section profiles of (a) surface morphology and (b)-(d) various energy densities, for 2.5% misfit and times $t = 1000$ (at early stage of instability and island formation), 2000 (island coarsening stage), and 10000 (saturating stage). Different components of the film surface chemical potential are shown, including the surface-energy contribution (dot-dashed orange curves), 1st-order elastic energy density $\mathcal{E}^{(1)f}$ (dashed black), 2nd-order elastic density $\mathcal{E}^{(2)f}$ (green stars), and the total elastic contribution $\mathcal{E}^f = \mathcal{E}^{(1)f} + \mathcal{E}^{(2)f}$ (solid brown).

of surface energy, showing as energy penalty for high-curvature surface areas and hence a spatial distribution opposite to that of elastic density (see the dot-dashed curves). This classical view of quantum dot formation has been well reproduced in our results of all three evolution stages: the early morphological instability shown in Fig. 11(b) (at $t = 1000$), a coarsening regime in Fig. 11(c) (at $t = 2000$), and a saturating stage in Fig. 11(d) (at $t = 10000$).

For islands to be saturated and stabilized, one would expect mechanisms of film evolution involving additional energy penalty for large, increasing island size, so that the overall stabilization factors would compensate and suppress the destabilization effect (i.e., continuing growth and coarsening of surface islands) caused by stress relaxation. In previous studies such factors are usually provided by additional surface energy terms particularly the surface energy anisotropy, which has been shown to enhance the surface-energy stabilization effect, constrain the island height, and lead to island shape/facet selection and transition^{16,17}; this effect of surface anisotropy has been deemed essential for the existence of steady island arrays in some previous theoretical work (with various assumptions of the wetting effect)^{26,32,36}. However, in this work we only consider isotropic surface energy. What we identify here is a new factor that is due to the contribution of higher-order perturbed elastic energy on the interaction and evolution of surface islands, as detailed in Fig. 11: Positive contribution from the 2nd-order elastic energy density $\mathcal{E}^{(2)f}$ is found for large surface islands, showing as an effective energy-penalty term and hence a reduction of strain relaxation effect. [Note that this result is still compatible with the well-known strain relaxation mechanism, since the total elastic density \mathcal{E}^f still shows a destabilization effect due to the dominance of 1st-order density $\mathcal{E}^{(1)f}$; see Figs. 11 (c) and (d).] Such effect of $\mathcal{E}^{(2)f}$ becomes important only at late stage with large enough islands, and is negligible for small ones, as seen from the comparison between Figs. 11 (b)-(d).

To understand this seemingly counterintuitive result which is beyond the conventional view based on linear instability analysis, we examine the detailed expression of $\mathcal{E}^{(2)f}$ which, from Eqs. (21)–(23), is rewritten as

$$\mathcal{E}^{(2)f}(\mathbf{r}) = \epsilon^{*2} \left[f(h) + \int d\mathbf{r}' \int d\mathbf{r}'' h(\mathbf{r}') G(\mathbf{r} - \mathbf{r}', \mathbf{r}' - \mathbf{r}'') h(\mathbf{r}'') \right], \quad (28)$$

where

$$f(h) = |\nabla h|^2 + \nu \left(\mathcal{E}^{(1)f} / \epsilon^{*2} \right)^2 + (1 - \nu) \sum_{i=1}^3 g_i^2(h), \quad (29)$$

with $g_i(h)$ ($i = 1, 2, 3$) the Fourier transform of $q_x^2 \hat{h}/q$, $q_y^2 \hat{h}/q$, and $\sqrt{2} q_x q_y \hat{h}/q$ respectively, and

$$G(\mathbf{r} - \mathbf{r}', \mathbf{r}' - \mathbf{r}'') = \sum_{\mathbf{q}, \mathbf{q}'} e^{i\mathbf{q} \cdot (\mathbf{r} - \mathbf{r}') + i\mathbf{q}' \cdot (\mathbf{r}' - \mathbf{r}'')} \\ \times \frac{2}{qq'} \left\{ q_x(q_x - q'_x)(q_x^2 + \nu q_y'^2) + q_y(q_y - q'_y)(q_y^2 + \nu q_x'^2) + (1 - \nu) q'_x q'_y [q_x(q_y - q'_y) + q_y(q_x - q'_x)] \right\}. \quad (30)$$

In Eq. (28), the first part $f(h)$ is always positive, analogous to the “self” elastic energy of a given surface profile that serves as a energy penalty to suppress its coarsening; the 2nd part represents the correlation between surface heights and thus the elastic interaction between surface islands. Within each island region (particularly near the peak), the magnitudes of both parts increase with the island size as verified in our numerical calculations.

If these 2nd-order elastic contributions are absent or not strong enough, the elastic energy relaxation would increasingly dominate over the surface-energy stabilization effect, driving the continuing island growth even in the presence of the wetting potential. This can be illustrated clearly from our numerical results given in Fig. 12, where the same film evolution equation (22) is simulated, but with only first-order elastic energy $\mathcal{E}^{(1)f}$ incorporated. All other parameters remain unchanged, including the same wetting potential approximation Eq. (3). The maximum surface height is found to increase monotonically with time [see Fig. 12 (a)], without any slowing or saturation process observed, a result that is consistent with previous work³⁴. Time evolution of the corresponding 2D cross-section surface profiles is given in Fig. 12 (b), from which two main features of surface dynamics can be identified: (1) Large mass transport from film layers to islands is observed, leading to much thinner film layers between surface islands as compared to the result shown in Fig. 11 (a) which incorporates the 2nd-order elastic energy effects. Although the wetting potential still has the effect of preserving the wetting layer in-between surface islands and then limiting the diffusion process from the depleted wetting layer to the peaks, here such effect becomes relatively weaker as time evolves due to the increasing dominance of the destabilization effect of 1st-order elastic energy and the absence of “self” energy penalty term $f(h)$ for large islands. (2) Mass transport between islands continues to occur, which corresponds to island migration or coarsening process and is actually a secondary effect compared to (1). This process cannot be prevented by the wetting effect, and can be controlled only by the higher-order elastic energy terms describing island interaction and correlation [see Eq. (28)]. Thus at late times the island heights increase rapidly, resulting in the formation of surface islands with large aspect ratio between height and width as shown in Fig. 12. The perturbation method used here is no longer valid for such high islands, and the simulations will ultimately blow up. This is qualitatively different from the results given above with the incorporation of 2nd-order elastic energy, where islands with well constrained aspect ratio are obtained which also shows the applicability of the perturbation method developed here.

All these results indicate that the nonlinearities given by the higher-order strain energy of individual islands and the elastic interaction between islands can affect the pathway of film strain relaxation at late evolution times, slow down the decrease of total elastic energy via their increasing positive energy contribution for large islands, and thus effectively reduce the effect of stress relaxation as the surface instability driving force. Such reduction leads to relatively stronger role played by the surface energy and the wetting potential at later times [see the comparison between Figs. 11 (c) and (d), and between Figs. 11 (a) and 12 (b)], limiting the mass transport between film layers and islands and hence suppressing the island growth and coarsening.

VIII. CONCLUSIONS

We have investigated the nonlinear dynamic processes governing the formation, coarsening, and stabilization of strained quantum dot islands on the surface of heteroepitaxial films, through the development of a nonlinear evolution equation for film morphology. Our study is based on a continuum elasticity model that incorporates the film-substrate wetting effect and importantly, on the construction of a perturbation method in Fourier space for determining the system elastic properties. In addition to a linear stability analysis which yields the conditions of film morphological instability, we have performed large scale numerical calculations of the dynamic equation derived to study the detailed behavior of film evolution. We focus on effects of small misfit strains which correspond to relatively large length scale of surface nanostructures, and analyze the evolution of strained surface islands/dots using a variety of characteristics of film morphology, including the structure factor of surface height, its first three moments, the maximum height of surface profile, and the surface roughness.

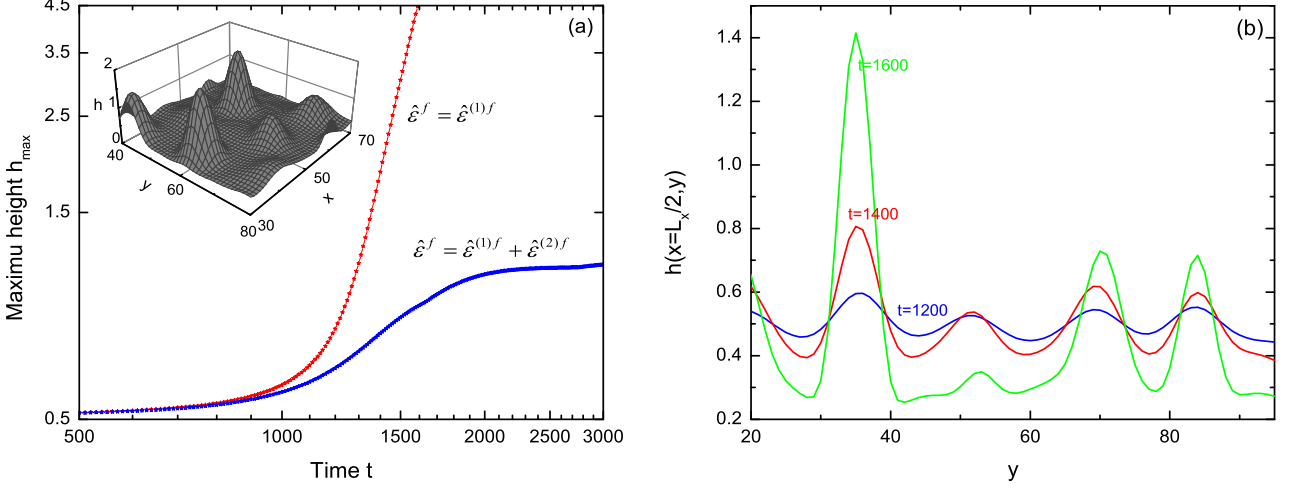


FIG. 12: Results of strained film evolution with only first-order elastic energy $\mathcal{E}^{(1)f}$ incorporated. All other parameters are the same as those in Figs. 10 and 11. (a) Maximum surface height as a function of time t , with results from calculations up to 2nd-order elastic energy (with $\mathcal{E}^f = \mathcal{E}^{(1)f} + \mathcal{E}^{(2)f}$) also shown for comparison; a sample 3D image of island morphology at $t = 1600$ is presented in the inset. (b) 2D cross-section profiles of film surface morphology at different times.

Consistent with previous experimental and theoretical work, our results have shown three characteristic stages of island evolution for post-deposited annealing films, including (1) the early stage of morphological instability and island formation, as characterized by the exponential growth of maximum structure factor S_{\max} and the surface roughness as well as the increase of maximum surface height and moments m_n ; (2) a nonlinear island coarsening stage, with a transient power-law behavior of m_n decay that appears at the beginning of this stage; and (3) a crossover to an asymptotic state of saturated island arrays (although without long-range spatial order), after the slowing and suppression process of coarsening. Also, the dependence of these detailed properties on the film-substrate misfit strain has been obtained, such as the values of coarsening exponents and the time ranges for the crossover between different evolution stages. These have been shown important for the understanding of different, or seemingly inconsistent, experimental results particularly for the late time stage of island coarsening or stabilization. On the other hand, such dependence does not qualitatively affect our results of the three evolution regimes; same conclusion can be drawn for the effect of different finite system sizes used in our simulations. To understand the mechanisms underlying the nonlinear evolution of strained films, we have examined the effects of film-substrate wetting potential, in particular its role on the suppression of the valley-to-peak mass diffusion process that would lead to wetting layer depletion, and its constraining effect on island growth. Furthermore, through a detailed study of time evolution of elastic energy density distribution at the film surface, we find that higher-order terms of film elastic energy, which incorporate the interaction between strained surface islands and the higher-order “self” elastic energy of individual islands, can effectively alter the relaxation pathway of film strain energy at late stage. They play an important role on the saturation and stabilization of quantum dot arrays, in particular the crossover to the saturated state with balanced multi-island interactions and limited island-layer and between-island mass transport. Thus our results indicate that both effects of film-substrate wetting interaction and high-order elastic energy are pivotal for the achieving of steady quantum dot arrays and also for the understanding of self-assembly process of strained film heteroepitaxy.

Acknowledgments

This work was supported by the National Science Foundation under Grant No. DMR-0845264.

Appendix: Third order perturbation results of film elasticity

As described in Sec. III, our perturbation approach developed here for solving the system elasticity problem can be extended to obtain higher order results through a recursive procedure. We have calculated the elastic properties of this heteroepitaxial system up to third order, with results presented in this appendix. The 3rd-order perturbed elastic energy density is given by

$$\begin{aligned} \tilde{\mathcal{E}}^{(3)f} = & \frac{E\epsilon}{1-\nu} \left[(1-\nu) \frac{a_1^{(3)} q_x + b_1^{(3)} q_y}{\mu q} - (1-2\nu) \frac{c_1^{(3)}}{2\mu} \right] \\ & + \sum_{\mathbf{q}'} \left\{ \frac{1+\nu}{2E} \left[\hat{\sigma}_{ij}^{(1)f}(\mathbf{q}') \hat{\sigma}_{ij}^{(2)f}(\mathbf{q}-\mathbf{q}') + \hat{\sigma}_{ij}^{(2)f}(\mathbf{q}') \hat{\sigma}_{ij}^{(1)f}(\mathbf{q}-\mathbf{q}') \right] \right. \\ & \left. - \frac{\nu}{2E} \left[\hat{\sigma}_{il}^{(1)f}(\mathbf{q}') \hat{\sigma}_{il}^{(2)f}(\mathbf{q}-\mathbf{q}') + \hat{\sigma}_{il}^{(2)f}(\mathbf{q}') \hat{\sigma}_{il}^{(1)f}(\mathbf{q}-\mathbf{q}') \right] \right\}, \end{aligned} \quad (\text{A.1})$$

where

$$a_1^{(3)} = \sum_{\mathbf{q}'} \left[(q_x - q'_x) \hat{\sigma}_{xx}^{(2)f}(\mathbf{q}') + (q_y - q'_y) \hat{\sigma}_{xy}^{(2)f}(\mathbf{q}') \right] \hat{h}(\mathbf{q}-\mathbf{q}'), \quad (\text{A.2})$$

$$b_1^{(3)} = \sum_{\mathbf{q}'} \left[(q_x - q'_x) \hat{\sigma}_{xy}^{(2)f}(\mathbf{q}') + (q_y - q'_y) \hat{\sigma}_{yy}^{(2)f}(\mathbf{q}') \right] \hat{h}(\mathbf{q}-\mathbf{q}'), \quad (\text{A.3})$$

$$c_1^{(3)} = \sum_{\mathbf{q}'} i \left[(q_x - q'_x) \hat{\sigma}_{xz}^{(2)f}(\mathbf{q}') + (q_y - q'_y) \hat{\sigma}_{yz}^{(2)f}(\mathbf{q}') \right] \hat{h}(\mathbf{q}-\mathbf{q}'). \quad (\text{A.4})$$

Based on the perturbation solutions of the system elasticity, we have obtained the first and second order results for elastic stress tensors at the film surface, which are used to calculate the perturbed elastic energy density given above. In second order we have

$$\begin{aligned} \hat{\sigma}_{xx}^{(2)f}(\mathbf{q}) = & -\frac{E\epsilon}{1-\nu} \sum_{\mathbf{q}'} \left\{ 4 \frac{q_x(q_x - q'_x)}{q^3 q'} (\nu q_y'^2 + q_x'^2) (q^2 + \nu q_y^2) + 4\nu \frac{(q_y - q'_y) q_y^3}{q^3 q'} (q_y'^2 + \nu q_x'^2) \right. \\ & + 4(1-\nu) \frac{q'_x q'_y}{q^3 q'} [q_x(q_y - q'_y) + q_y(q_x - q'_x)] (q_y^2 + \nu q_x^2) - \frac{1}{q^2} [q'_x(q_x - q'_x) + q'_y(q_y - q'_y)] (2\nu q_y^2 + q_x^2) \\ & \left. + 4(1-\nu) \frac{q_x q_y q'_x q'_y}{q^3 q'} [q_y(q_y - q'_y) - q_x(q_x - q'_x)] \right\} \hat{h}(\mathbf{q}') \hat{h}(\mathbf{q}-\mathbf{q}'), \end{aligned} \quad (\text{A.5})$$

$$\begin{aligned} \hat{\sigma}_{yy}^{(2)f}(\mathbf{q}) = & -\frac{E\epsilon}{1-\nu} \sum_{\mathbf{q}'} \left\{ 4 \frac{q_y(q_y - q'_y)}{q^3 q'} (\nu q_x'^2 + q_y'^2) (q^2 + \nu q_x^2) + 4\nu \frac{(q_x - q'_x) q_x^3}{q^3 q'} (q_x'^2 + \nu q_y'^2) \right. \\ & + 4(1-\nu) \frac{q'_x q'_y}{q^3 q'} [q_x(q_y - q'_y) + q_y(q_x - q'_x)] (q_y^2 + \nu q_x^2) - \frac{1}{q^2} [q'_x(q_x - q'_x) + q'_y(q_y - q'_y)] (2\nu q_x^2 + q_y^2) \\ & \left. - 4(1-\nu) \frac{q_x q_y q'_x q'_y}{q^3 q'} [q_y(q_y - q'_y) - q_x(q_x - q'_x)] \right\} \hat{h}(\mathbf{q}') \hat{h}(\mathbf{q}-\mathbf{q}'), \end{aligned} \quad (\text{A.6})$$

$$\hat{\sigma}_{zz}^{(2)f}(\mathbf{q}) = \frac{E\epsilon}{(1-\nu)} (3-2\nu) \sum_{\mathbf{q}'} [q'_x(q_x - q'_x) + q'_y(q_y - q'_y)] \hat{h}(\mathbf{q}') \hat{h}(\mathbf{q}-\mathbf{q}'), \quad (\text{A.7})$$

$$\begin{aligned} \hat{\sigma}_{xy}^{(2)f}(\mathbf{q}) = & E\epsilon \sum_{\mathbf{q}'} \left\{ -4 \frac{q_x q_y}{q' q^3} [(q_x(q_x - q'_x)(q_y'^2 + \nu q_x'^2) + q_y(q_y - q'_y)(q_y'^2 + \nu q_x'^2)) \right. \\ & + (1-\nu) q'_x q'_y (q_x(q_y - q'_y) + q_y(q_x - q'_x))] + \frac{(1-2\nu) q_x q_y}{(1-\nu) q^2} [q'_x(q_x - q'_x) + q'_y(q_y - q'_y)] \\ & - \frac{4}{(1-\nu) q^3 q'} [q_y(q_x - q'_x)(q_x'^2 + \nu q_y'^2) - q_x(q_y - q'_y)(q_y'^2 + \nu q_x'^2) \\ & \left. + (1-\nu) q'_x q'_y (q_y(q_y - q'_y) - q_x(q_x - q'_x))] \right\} \hat{h}(\mathbf{q}') \hat{h}(\mathbf{q}-\mathbf{q}'), \end{aligned} \quad (\text{A.8})$$

$$\begin{aligned}
\hat{\sigma}_{xz}^{(2)f}(\mathbf{q}) &= \frac{2E\epsilon}{1-\nu} \sum_{\mathbf{q}'} i \frac{q_x}{q^2 q'} \{q_x(q_x - q'_x)(q_x'^2 + \nu q_y'^2) + q_y(q_y - q'_y)(q_y'^2 + \nu q_x'^2) \\
&\quad + (1-\nu)q'_x q'_y [q_x(q_y - q'_y) + q_y(q_x - q'_x)] - \frac{q_y^2}{q_x} [(q_x - q'_x)(q_x'^2 + \nu q_y'^2) + (1-\nu)(q_y - q'_y)q'_x q'_y] \\
&\quad + (1-\nu)q_y(q_x - q'_x)q'_x q'_y + q_y(q_y - q'_y)(q_y'^2 + \nu q_x'^2)\} \hat{h}(\mathbf{q}') \hat{h}(\mathbf{q} - \mathbf{q}'), \tag{A.9}
\end{aligned}$$

$$\begin{aligned}
\hat{\sigma}_{yz}^{(2)f}(\mathbf{q}) &= \frac{2E\epsilon}{1-\nu} \sum_{\mathbf{q}'} i \frac{q_y}{q^2 q'} \{q_x(q_x - q'_x)(q_x'^2 + \nu q_y'^2) + q_y(q_y - q'_y)(q_y'^2 + \nu q_x'^2) \\
&\quad + (1-\nu)q'_x q'_y [q_x(q_y - q'_y) + q_y(q_x - q'_x)] - \frac{q_x^2}{q_y} [(q_y - q'_y)(q_y'^2 + \nu q_x'^2) + (1-\nu)(q_x - q'_x)q'_x q'_y] \\
&\quad + (1-\nu)q_x(q_y - q'_y)q'_x q'_y + q_x(q_x - q'_x)(q_x'^2 + \nu q_y'^2)\} \hat{h}(\mathbf{q}') \hat{h}(\mathbf{q} - \mathbf{q}'), \tag{A.10}
\end{aligned}$$

while the results for first order perturbation are given by

$$\hat{\sigma}_{xx}^{(1)f}(\mathbf{q}) = \frac{2E\epsilon}{q(1-\nu)} (q_x^2 + \nu q_y^2) \hat{h}(\mathbf{q}), \tag{A.11}$$

$$\hat{\sigma}_{yy}^{(1)f}(\mathbf{q}) = \frac{2E\epsilon}{q(1-\nu)} (q_y^2 + \nu q_x^2) \hat{h}(\mathbf{q}), \tag{A.12}$$

$$\hat{\sigma}_{zz}^{(1)f}(\mathbf{q}) = 0, \tag{A.13}$$

$$\hat{\sigma}_{xy}^{(1)f}(\mathbf{q}) = 2E\epsilon \frac{q_x q_y}{q} \hat{h}(\mathbf{q}), \tag{A.14}$$

$$\hat{\sigma}_{xz}^{(1)f}(\mathbf{q}) = -\frac{E\epsilon}{1-\nu} i q_x \hat{h}(\mathbf{q}), \tag{A.15}$$

$$\hat{\sigma}_{yz}^{(1)f}(\mathbf{q}) = -\frac{E\epsilon}{1-\nu} i q_y \hat{h}(\mathbf{q}). \tag{A.16}$$

- ¹ J. Stangl, V. Holy, and G. Bauer, Rev. Mod. Phys. **76**, 725 (2004).
- ² S. Kiravittaya, A. Rastelli, and O. G. Schmidt, Rep. Prog. Phys. **72**, 046502 (2009).
- ³ I. Berbezier and A. Ronda, Surf. Sci. Rep. **64**, 47 (2009).
- ⁴ R. J. Asaro and W. A. Tiller, Metall. Trans. **3**, 1789 (1972); M. A. Grinfeld, Sov. Phys. Dokl. **31**, 831 (1986).
- ⁵ D. J. Srolovitz, Acta Metall. **37**, 621 (1989).
- ⁶ B. J. Spencer, P. W. Voorhees, and S. H. Davis, Phys. Rev. Lett. **67**, 3696 (1991); J. Appl. Phys. **73**, 4955 (1993).
- ⁷ P. Sutter and M. G. Lagally, Phys. Rev. Lett. **84**, 4637 (2000).
- ⁸ R. M. Tromp, F. M. Ross, and M. C. Reuter, Phys. Rev. Lett. **84**, 4641 (2000).
- ⁹ J. Tersoff, B. J. Spencer, A. Rastelli, and H. von Känel, Phys. Rev. Lett. **89**, 196104 (2002).
- ¹⁰ J. E. Guyer and P. W. Voorhees, Phys. Rev. Lett. **74**, 4031 (1995).
- ¹¹ B. J. Spencer, P. W. Voorhees, and J. Tersoff, Phys. Rev. B **64**, 235318 (2001).
- ¹² Z.-F. Huang and R. C. Desai, Phys. Rev. B **65**, 205419 (2002); **65**, 195421 (2002).
- ¹³ R. C. Desai, H. K. Kim, A. Chatterji, D. Ngai, S. Chen, and N. Yang, Phys. Rev. B **81**, 235301 (2010).
- ¹⁴ L. E. Shilkrot, D. J. Srolovitz, and J. Tersoff, Phys. Rev. B **62**, 8397 (2000); **67**, 249901(E) (2003).
- ¹⁵ Z.-F. Huang and R. C. Desai, Phys. Rev. B **67**, 075416 (2003); Z.-F. Huang, D. Kandel, and R. C. Desai, Appl. Phys. Lett. **82**, 4705 (2003).
- ¹⁶ F. M. Ross, J. Tersoff, and R. M. Tromp, Phys. Rev. Lett. **80**, 984 (1998).
- ¹⁷ G. Medeiros-Ribeiro, T. I. Kamins, D. A. A. Ohlberg, and R. S. Williams, Phys. Rev. B **58**, 3533 (1998).
- ¹⁸ A. Rastelli, M. Stoffel, J. Tersoff, G. S. Kar, and O. G. Schmidt, Phys. Rev. Lett. **95**, 026103 (2005).
- ¹⁹ M. R. McKay, J. A. Venables, and J. Drucker, Phys. Rev. Lett. **101**, 216104 (2008).
- ²⁰ J. A. Floro, M. B. Sinclair, E. Chason, L. B. Freund, R. D. Twisten, R. Q. Hwang, and G. A. Lucadamo, Phys. Rev. Lett. **84**, 701 (2000).
- ²¹ T. J. Krzyzewski and T. S. Jones, J. Appl. Phys. **96**, 668 (2004).
- ²² W. Dorsch, H. P. Strunk, H. Wawra, G. Wagner, J. Groenen, and R. Carles, Appl. Phys. Lett. **72**, 179 (1998).
- ²³ W. H. Yang and D. J. Srolovitz, Phys. Rev. Lett. **71**, 1593 (1993).
- ²⁴ B. J. Spencer, S. H. Davis, and P. W. Voorhees, Phys. Rev. B, **47**, 9760 (1993).
- ²⁵ B. J. Spencer and D. I. Meiron, Acta Metall. Mater. **42**, 3629 (1994).

- ²⁶ C.-H. Chiu, Appl. Phys. Lett. **75**, 3473 (1999); C.-H. Chiu and Z. Huang, J. Appl. Phys. **101**, 113540 (2007).
- ²⁷ F. Liu, A. H. Li, and M. G. Lagally, Phys. Rev. Lett. **87**, 126103 (2001).
- ²⁸ Y. Xiang and W. E, J. Appl. Phys. **91**, 9414 (2002).
- ²⁹ P. Liu, Y. W. Zhang, and C. Lu, Phys. Rev. B **68**, 035402 (2003).
- ³⁰ A. A. Golovin, S. H. Davis, and P. W. Voorhees, Phys. Rev. E **68**, 056203 (2003).
- ³¹ W. T. Tekalign and B. J. Spencer, J. Appl. Phys. **96**, 5505 (2004); **102**, 073503 (2007).
- ³² H. R. Eisenberg and D. Kandel, Phys. Rev. B, **71**, 115423 (2005).
- ³³ Y. Pang and R. Huang, Phys. Rev. B **74**, 075413 (2006).
- ³⁴ M. S. Levine, A. A. Golovin, S. H. Davis, and P. W. Voorhees, Phys. Rev. B **75**, 205312 (2007).
- ³⁵ J.-N. Aqua, T. Frisch, and A. Verga, Phys. Rev. B **76**, 165319 (2007); Phys. Rev. E **81**, 021605 (2010).
- ³⁶ J.-N. Aqua and T. Frisch, Phys. Rev. B **82**, 085322 (2010).
- ³⁷ J. Müller and M. Grant, Phys. Rev. Lett. **82**, 1736 (1999).
- ³⁸ K. Kassner, C. Misbah, J. Müller, J. Kappey, and P. Kohlert, Phys. Rev. E **63**, 036117 (2001).
- ³⁹ G. Nandipati and J. G. Amar, Phys. Rev. B **73**, 045409 (2006).
- ⁴⁰ T. P. Schulze and P. Smereka, J. Mech. Phys. Solids **57**, 521 (2009).
- ⁴¹ X. B. Niu, G. B. Stringfellow, and F. Liu, Phys. Rev. Lett. **107**, 076101 (2011).
- ⁴² K. R. Elder, M. Katakowski, M. Haataja, and M. Grant, Phys. Rev. Lett. **88**, 245701 (2002).
- ⁴³ Z.-F. Huang and K. R. Elder, Phys. Rev. Lett. **101**, 158701 (2008); Phys. Rev. B **81**, 165421 (2010).
- ⁴⁴ K.-A. Wu and P. W. Voorhees, Phys. Rev. B **80**, 125408 (2009).
- ⁴⁵ K. R. Elder, Z.-F. Huang, and N. Provatas, Phys. Rev. E **81**, 011602 (2010); K. R. Elder and Z.-F. Huang, J. Phys.: Condens. Matter **22**, 364103 (2010); Z.-F. Huang, K. R. Elder, and N. Provatas, Phys. Rev. E **82**, 021605 (2010).
- ⁴⁶ M. C. Cross, D. I. Meiron, and Y. Tu, Chaos **4**, 607 (1994).
- ⁴⁷ C. Sagui and R. C. Desai, Phys. Rev. E, **49**, 2225 (1994).